Supplemental information

Crystalline/Amorphous $Co_3(PO_4)_2$-MoO_{3-x}/NF Heterojunction

Synergistically Improves Overall Water Splitting Kinetics

Yi Chen[a], Hui Wang[a]*

[a]School of Materials Science & Engineering, South China University of Technology, Guangzhou 510640, China
Corresponding authors E-mail: wanghui@scut.edu.cn(H. Wang).

Table of Contents

1 Supporting experimental section

1.1. Chemicals and materials

Nickel foam (NF, 1 mm) and Pt/C (20 wt%) were purchased from Suzhou Sinero Technology Co., Ltd, $Co(NO_3)_2 \cdot 6H_2O$, $(NH_4)_6Mo_7O_{24} \cdot 4H_2O$, $CO(NH_2)_2$ (urea), NH_4F, ethanol, acetone, HCl, KOH, RuO_2 were purchased from Macklin. All chemicals were used as received without further purification.

1.2. Pretreatment of nickel foam

To remove oxides and grease from the nickel foam, the NF was sonicated in acetone, hydrochloric acid, anhydrous ethanol, and deionized water for 15 minutes, then vacuum-dried and prepared for use.

1.3. Synthesis of $Co_3(PO_4)_2$-MoO_{3-x}/NF

Briefly, 3.0 m mol $Co(NO_3)_2 \cdot 6H_2O$, 2 m mol $(NH_4)_6Mo_7O_{24} \cdot 4H_2O$, $CO(NH_2)_2$ (1 m mol) which provided an alkaline environment and NH_4F (3 m mol) which controled the morphology were completely dissolved in 30 mL of deionized water to form a red clear solution. This was then transferred to a 50 mL Teflon-lined autoclave and the pre-treated nickel foam was added. After being kept at 120℃ for 12h, Co_3O_4-MoO_{3-x}/NF was obtained after natural cooling. The obtained Co_3O_4-MoO_{3-x}/NF sample was then calcined under a 350°C hydrogen-argon mixture (5%H_2-Ar) atmosphere at a heating rate of 2°C/min for 2 h with sodium hypophosphite as phosphorus source. After this low-temperature phosphating reaction, Co_3O_4-MoO_{3-x}/NF was successfully transformed into the crystalline/amorphous $Co_3(PO_4)_2$-MoO_{3-x}/NF heterostructure.

1.4. Synthesis of $Co_3(PO_4)_2$ /NF, P-MoO_{3-x}/NF and Ni_2P/NF

The preparation was identical to that of $Co_3(PO_4)_2$-MoO_{3-x}/NF, except that in the first step $(NH_4)_6Mo_7O_{24}$-$4H_2O$ was not introduced as a source of Mo, $Co(NO_3)_2$-$6H_2O$ was not introduced as a source of Co, and neither was added.

1.5. Synthesis of electrodes of Pt/C and RuO_2 on nickel foam

10 mg Pt/C (20 wt%) and 40 μL Nafion (5 wt%) were dispersed in a mixture of 200 μL isopropyl alcohol and 800 μL deionized water and treated with ultrasound for 30 min. Then, 200 μL of catalyst inks was slowly loaded onto a clean surface of NF (1 mm $\times$ 1 mm) and dried in air. The catalyst loading of the Pt/C/NF catalyst is about 2.0 mg/cm^{-2}. At the same time, the RuO_2 electrode was prepared using the same method.

1.6 Materials Characterizations

The morphology and structure of samples were characterized by scanning electron microscopy (SEM, SU8600, 5k eV) Low-magnification and high-resolution transition electron microscopy (TEM) images were obtained from a TEM (Talos F200S, 200k eV) equipped with an energy diffraction spectroscopy (EDS). X-ray diffraction (XRD) measurements were conducted on a D/max 2500pc diffractometer with a monochromatic Cu Kα radiation (λ=1.54178 Å). The Raman spectra were collected on a (Renishaw) Raman spectrometer using a 450 nm laser，and X-ray photoelectron

spectroscopy (XPS) was performed on a thermal ECSALAB 250 (15keV, 6 mA) with an Al anode. All the charge states were compensated by shifting binding energies based on the C 1s peak (284.8 eV)。

1.7 Electrochemical measurements

The traditional standard three-electrode system was used for electrochemical testing. Specifically, the graphite rod was used as the counter electrode, the Hg/HgO electrode as the reference electrode, and the $Co_3(PO_4)_2$-MoO_{3-x}/NF as the working electrode. In particular, to obtain more accurate and reasonable data, all samples were activated for 200 cycles at a scan rate of 20 mV/s before the polarisation curve of the samples was measured. HER and OER measurements were carried out in 1 M KOH solution and before testing, N_2 and O_2 were passed through until the solution was saturated, respectively. In addition, to characterize the catalytic performance of the samples, polarisation curves were recorded at a scan rate of 2 mV/s and the measured potentials were converted to the reversible hydrogen electrode ERHE according to the equation $E_{RHE}=E_{Hg/HgO} + 0.098$ V $+ 0.0592 \times$ pH, with the polarisation potentials of the resulting samples corrected by 80% (except for total hydrolysis). The EIS spectra of each electrode material were collected at an overpotential of 100 mV, with a frequency range of $10^{-1} - 10^{-5}$ Hz and an amplitude of 10 mV. Stability tests were carried out using the chronopotentiometry (i-t), multipotential step, and voltammetric cycling methods. Specifically, the stability tests were performed at polarisation voltages with current densities of 10 mA cm^{-2} and 100 mA cm-2, respectively, and the samples were cycled for 3600 revolutions at a scan rate of 50 mV/s. The polarization curves of the 1st and 3601st cycles were recorded for comparison.

1.8 Electrochemical active surface area (ECSA)

The electrochemical active area (ECSA) of all catalysts was estimated based on the capacitance of the double electric layer (C_{dl}). Specifically, cyclic voltammetry curves were obtained at different scanning speeds (10, 20, 30, 40, and 50 mV/s) in the illegal pull-down interval of open-circuit voltage ± 50 mV. Then plotted the current density difference (Δj) between anodic and cathodic currents at fixed potential against the scan rate. The slope of the fit gives twice the C_{dl}, which was linearly related to ECSA. The formula was calculated as follows:

$$ECSA = \frac{C_{dl}}{C_s}$$

Where C_s refers to the specific capacitance of the sample measured under the same conditions, its value range was related to the nature of the electrolyte, in the acid electrolyte C_s value range was generally $0.015 \sim 0.110$ $mF\ cm^{-2}$, alkaline electrolyte C_s value range was generally: $0.022 \sim 0.130$ $0.022 \sim 0.130$ $mF\ cm^{-2}$[1].In general, for the purpose of comparing the magnitude of ECSA for different catalysts, C_s was taken

to be 0.035 mF in the acidic electrolyte and C_s in the basic electrolyte was taken to be

$0.040 \ mF \ cm^{-2}$[2].
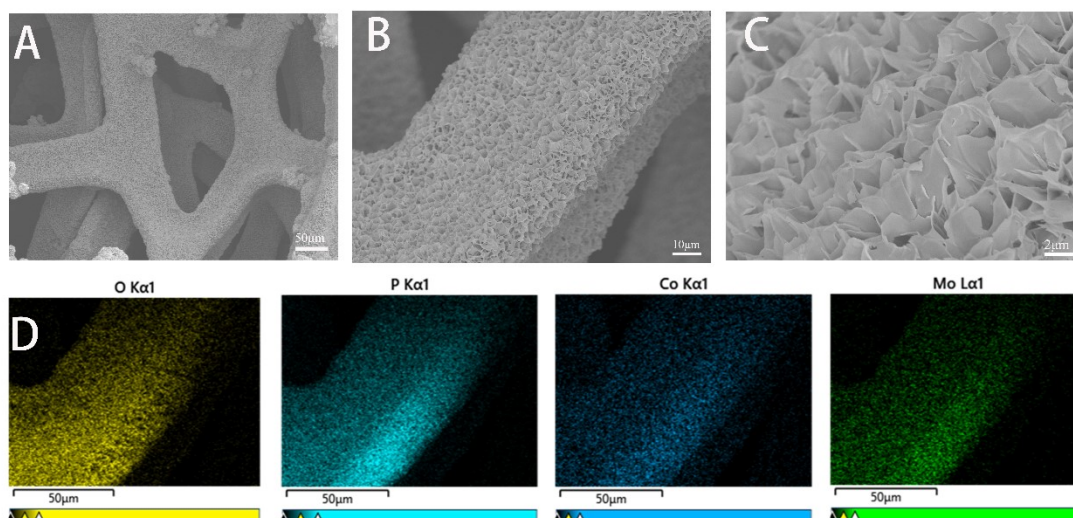
2. Supporting figures

Figure S1. (A-C) SEM images of Crystalline/amorphous $Co_3(PO_4)_2$-MoO_{3-x}/NF at different magnifications; (D) EDS images of Crystalline/amorphous $Co_3(PO_4)_2$-MoO_{3-x}/NF.
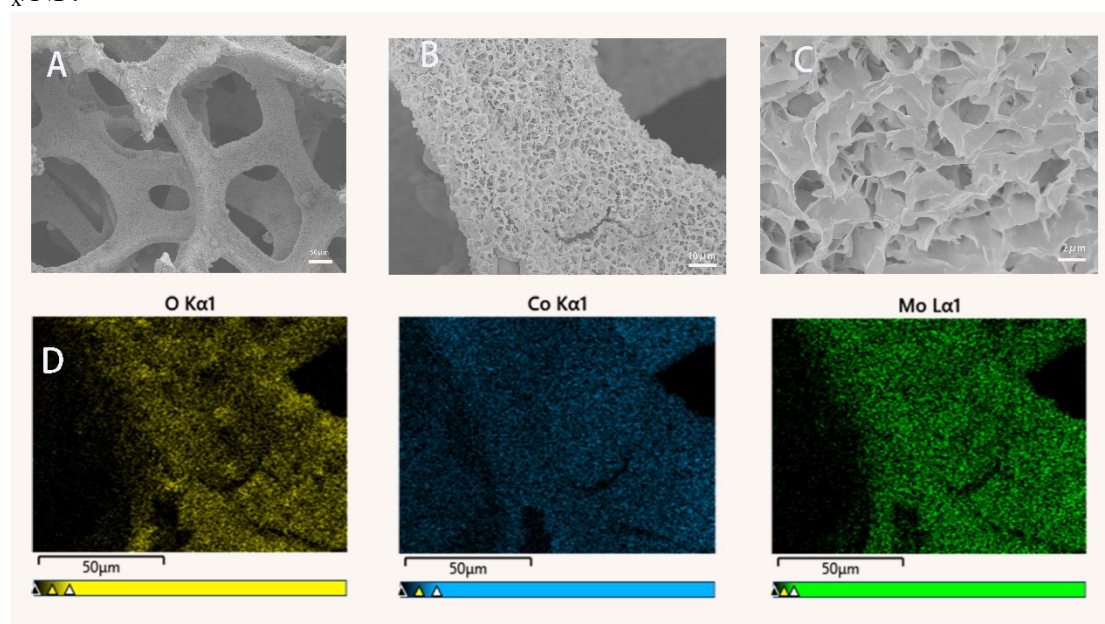
Figure S2. (A-C) SEM images of Co_3O_4-MoO_{3-x}/NF at different magnifications; (D) EDS images of Co_3O_4-MoO_{3-x}/NF.

P Kα1   O Kα1   Mo Lα1

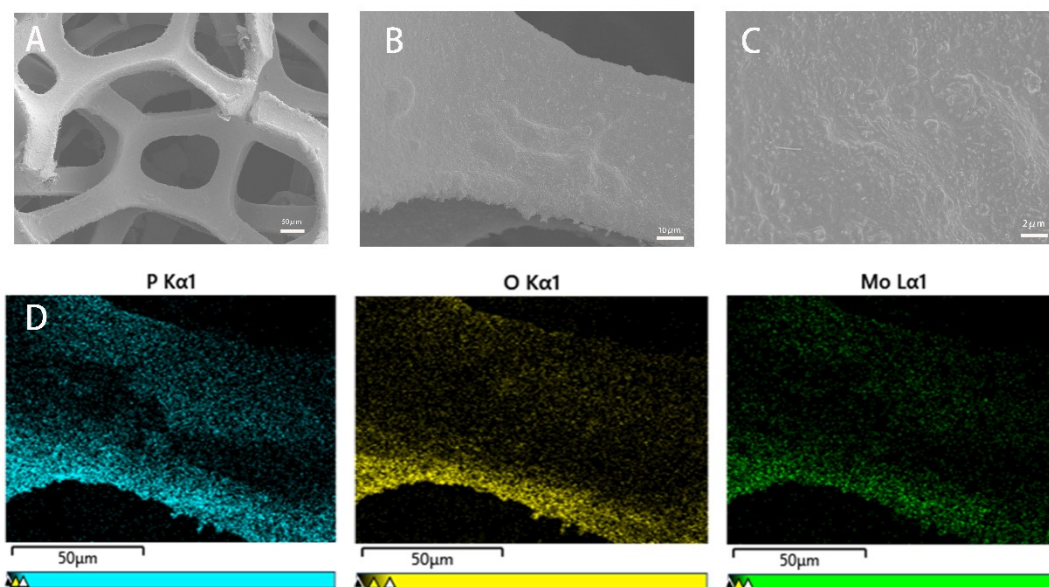**Figure S3.** (A-C) SEM images of amorphous P-MoO$_{3-x}$/NF at different magnifications; (D) EDS images of amorphous P-MoO$_{3-x}$/NF.
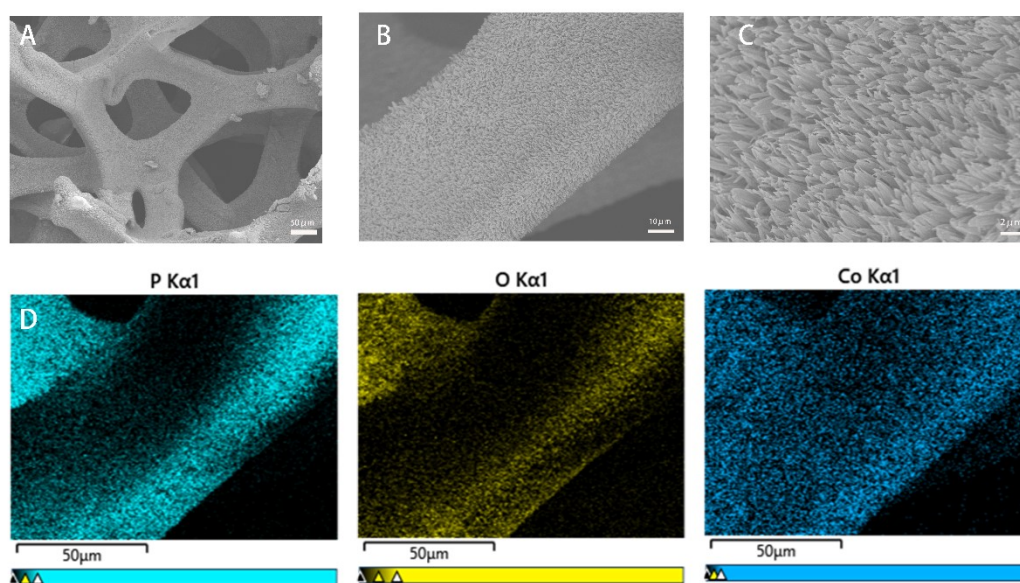

P Kα1   O Kα1   Co Kα1

Figure S4. (A-C) SEM images of crystalline Co$_3$(PO$_4$)$_2$/NF at different magnifications; (D) EDS images of crystalline Co$_3$(PO$_4$)$_2$/NF.
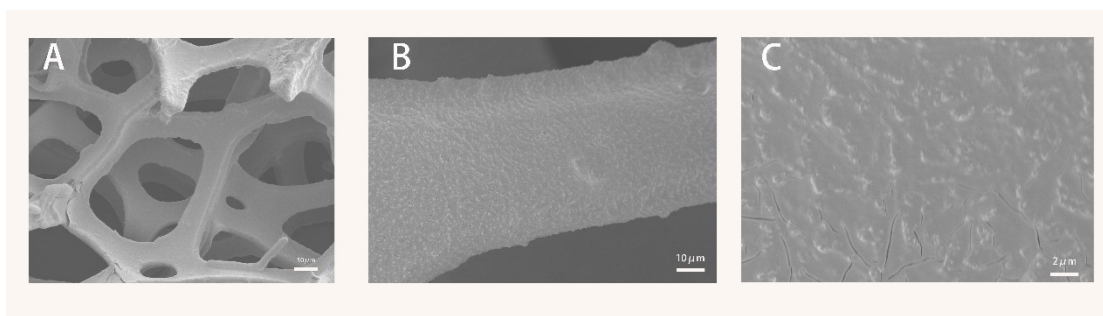
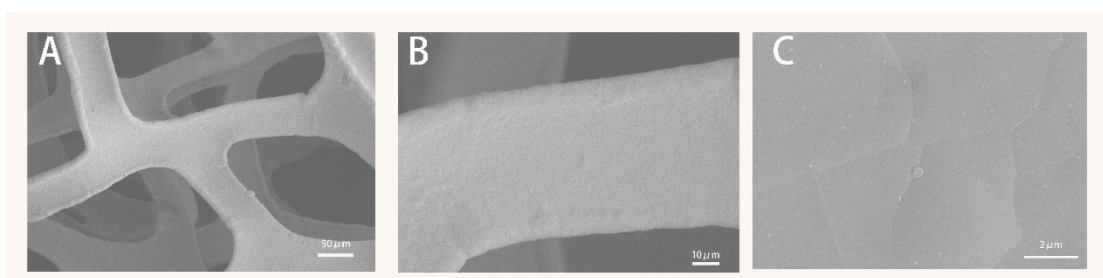**Figure S5.** (A-C) SEM images of Ni$_2$P/NF at different magnifications.

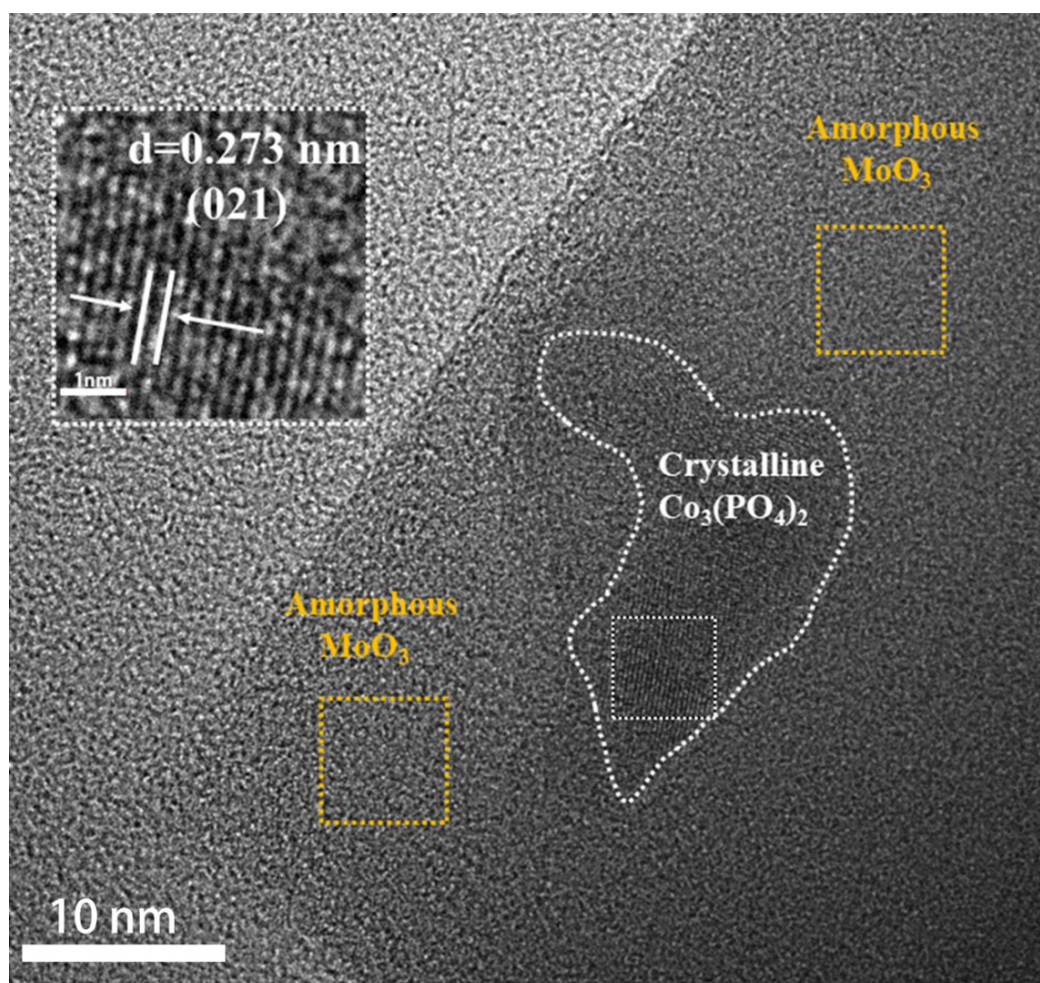**Figure S6**. (A-C) SEM images of crystalline bare NF at different magnifications.

Figure S7. HRTEM images of Co$_3$(PO$_4$)$_2$-MoO$_{3-x}$/NF.
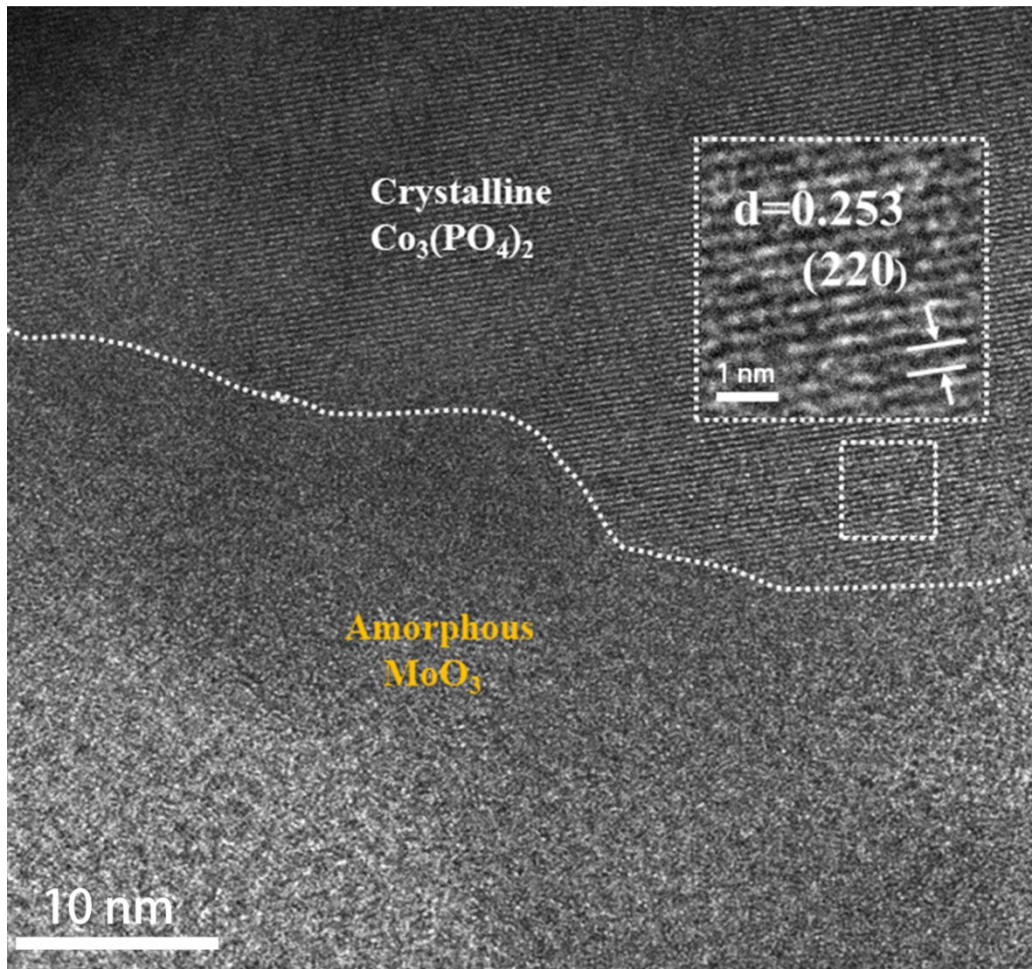
Figure S8. HRTEM images of $Co_3(PO_4)_2$-MoO_{3-x}/NF.
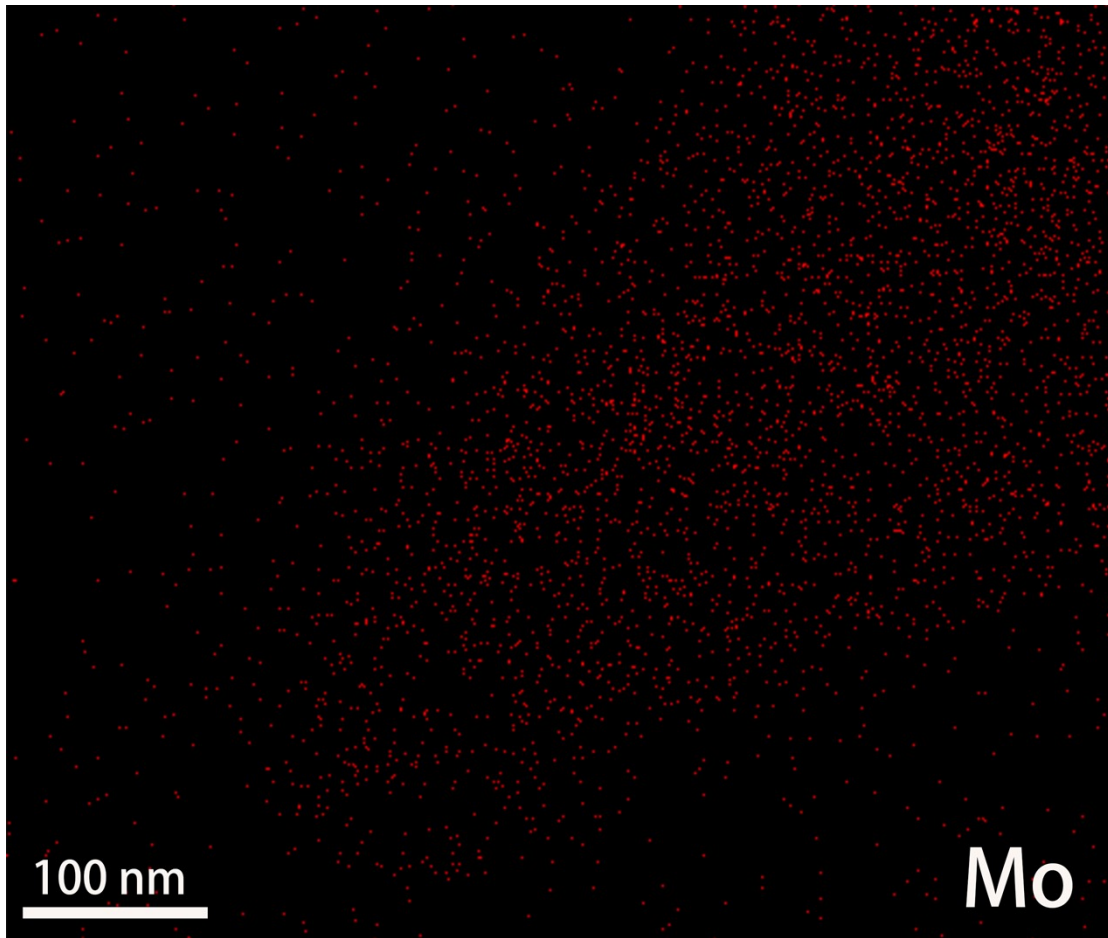
Figure S9. Element mapping diagram for element Mo.
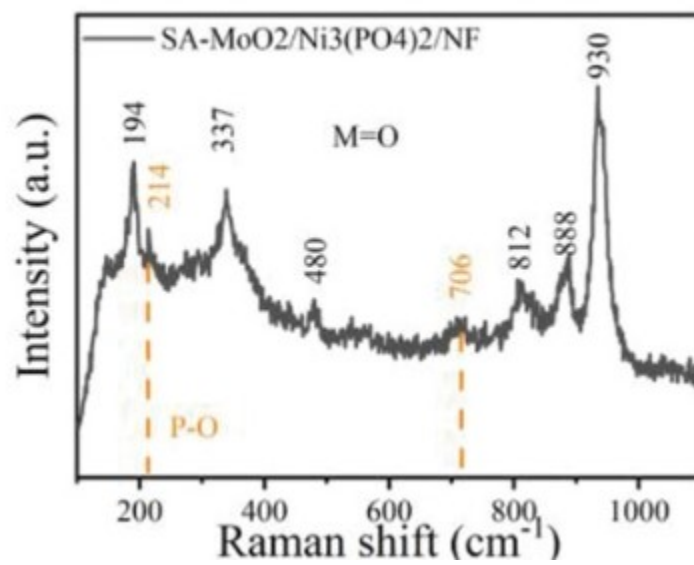
Figure S10. Raman spectra of $MoO_2/Ni_3(PO_4)_2$[3]

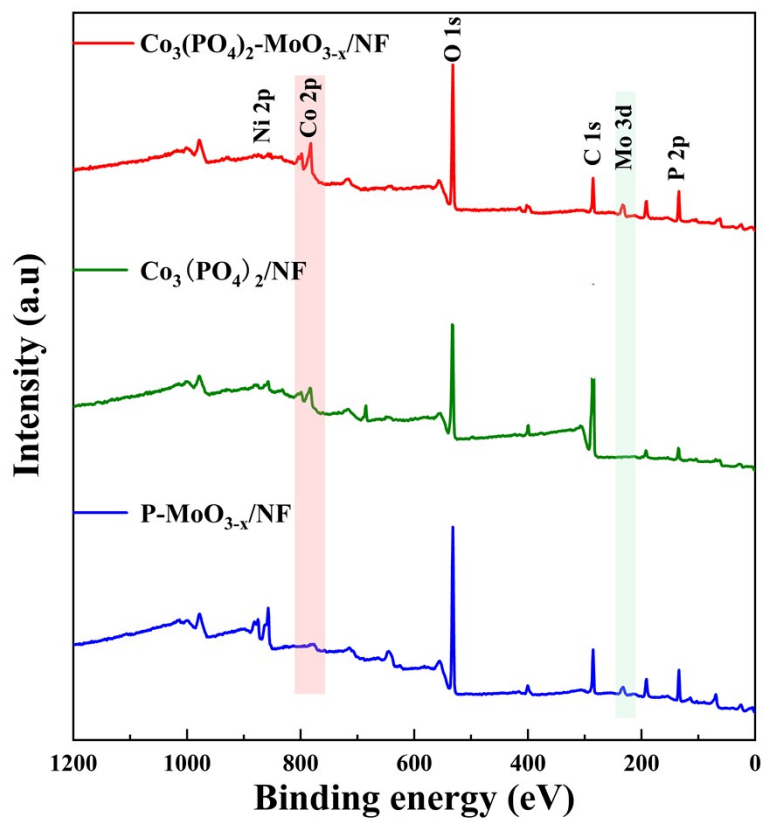**Figure S11.** Total spectrum of XPS measurements.

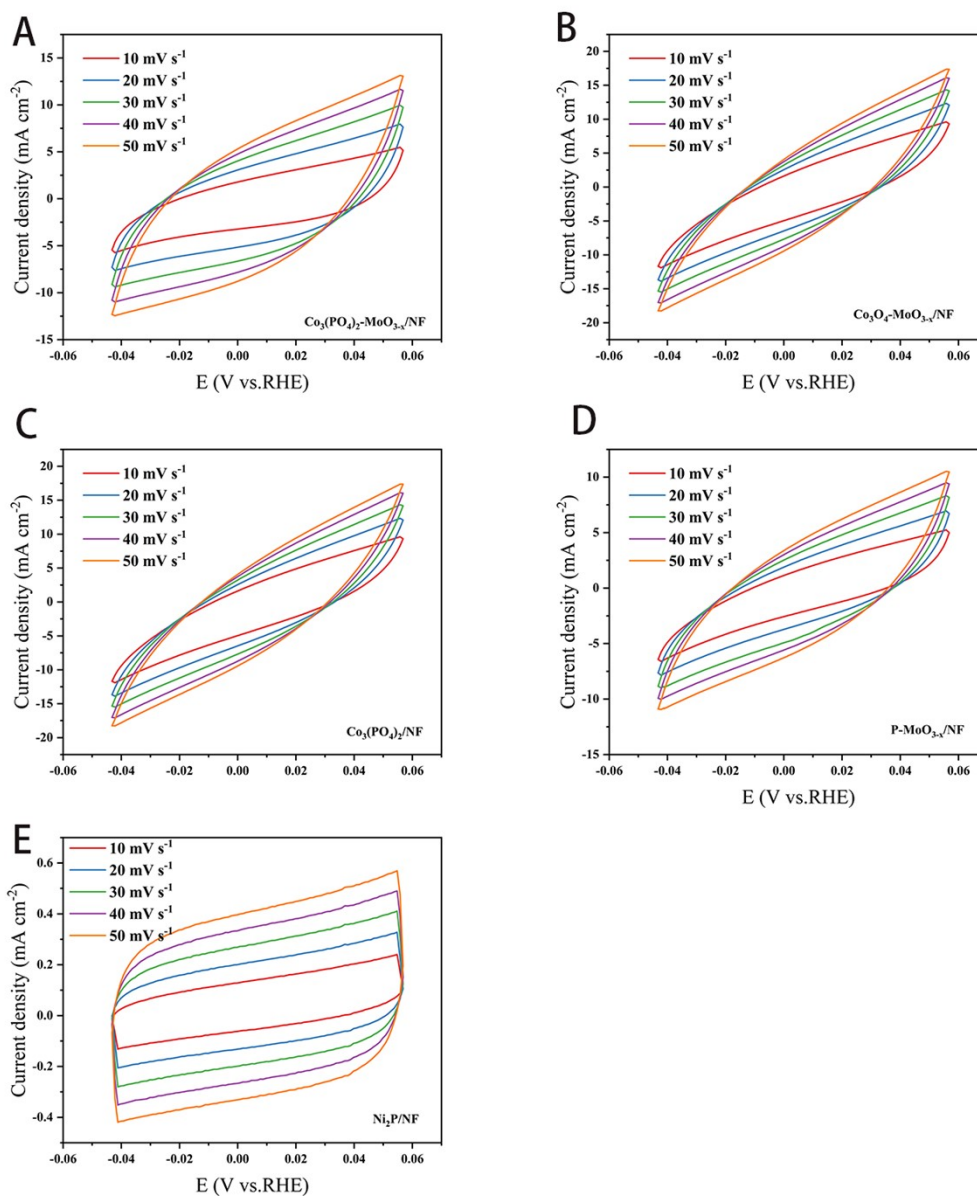**Figure S12.** In the HER test, Cyclic voltammograms (CV) curves for (A) Crystalline/amorphous $Co_3(PO_4)_2$-MoO_{3-x}/NF, (B) Co_3O_4-MoO_{3-x}/NF, (C) crystalline $Co_3(PO_4)_2$/NF, (D) amorphous P-MoO_{3-x}/NF, and(E) Ni_2P/NF between -0.05 to 0.05 V vs RHE at five different scan rates (10, 20, 30, 40, and 50 mV/s).

Figure S13. Polarization curves were recorded from $Co_3(PO_4)_2$-MoO_{3-x}/NF heterostructure for HER at a scan rate of 2mV/s initial (red curve) and after (blue curve) the chronopotentiometry test. The current densities corresponding to A and B are 10 and 100 mA cm^{-2} respectively.

Figure S14. Polarization curves were recorded from $Co_3(PO_4)_2$-MoO_{3-x}/NF heterostructure for HER at a scan rate of 2mV/s initial (red curve) and after (blue curve) the Multistep chronopotentiometry test.

Figure S15. The SEM image of the $Co_3(PO_4)_2$-MoO_{3-x}/NF heterojunction was obtained after the HER stability test.
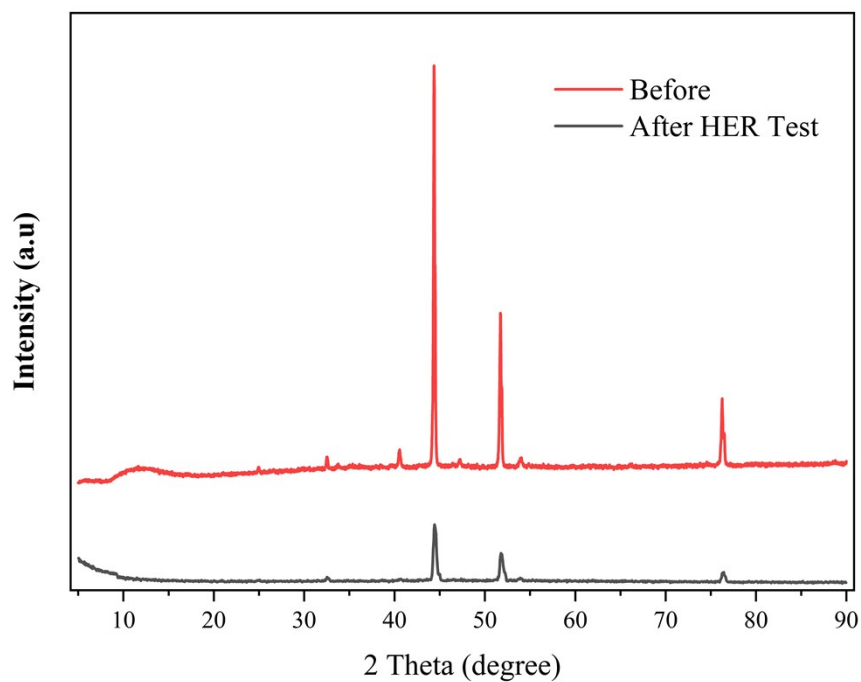
Figure S16. The XRD image of the $Co_3(PO_4)_2$-MoO_{3-x}/NF heterojunction was obtained after the HER stability test.
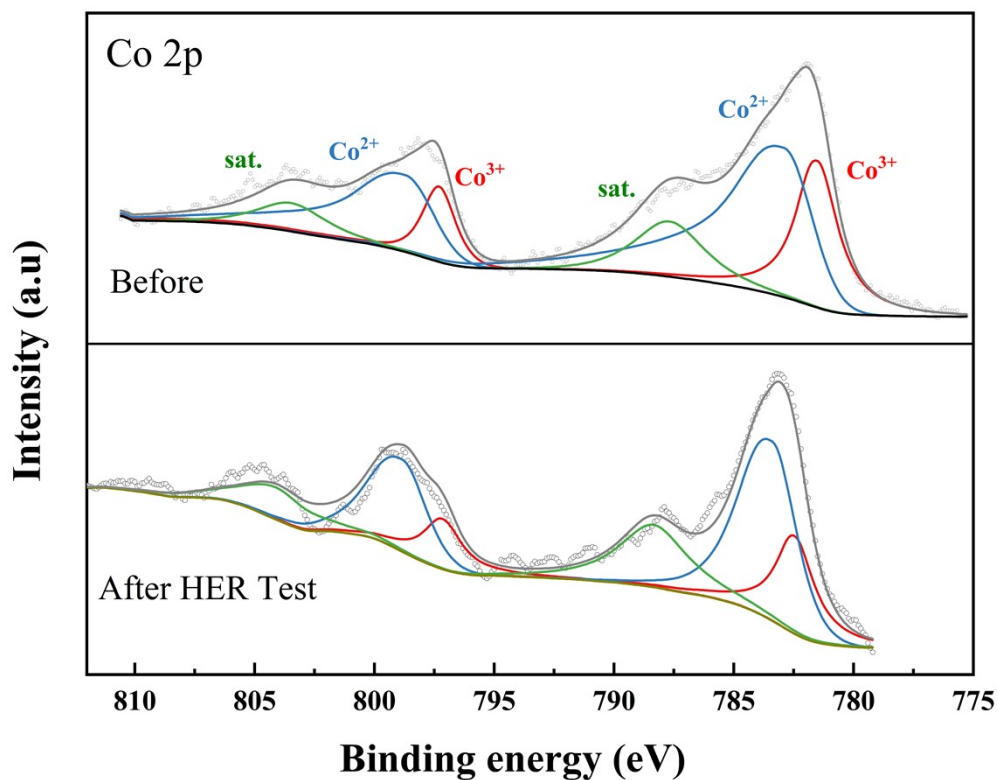
Figure S17. High-resolution XPS spectra of Co 2p for $Co_3(PO_4)_2$-MoO_{3-x}/NF after the HER stability test.
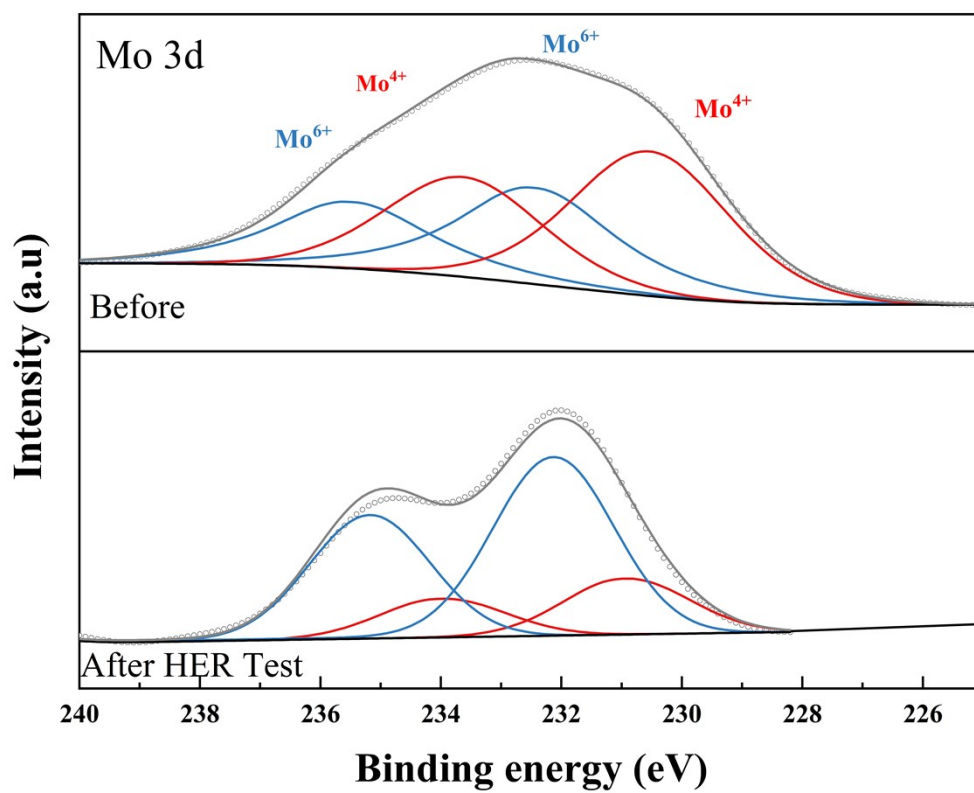
Figure S18. High-resolution XPS spectra of Mo 3d for $Co_3(PO_4)_2$-MoO_{3-x}/NF after the HER stability test.
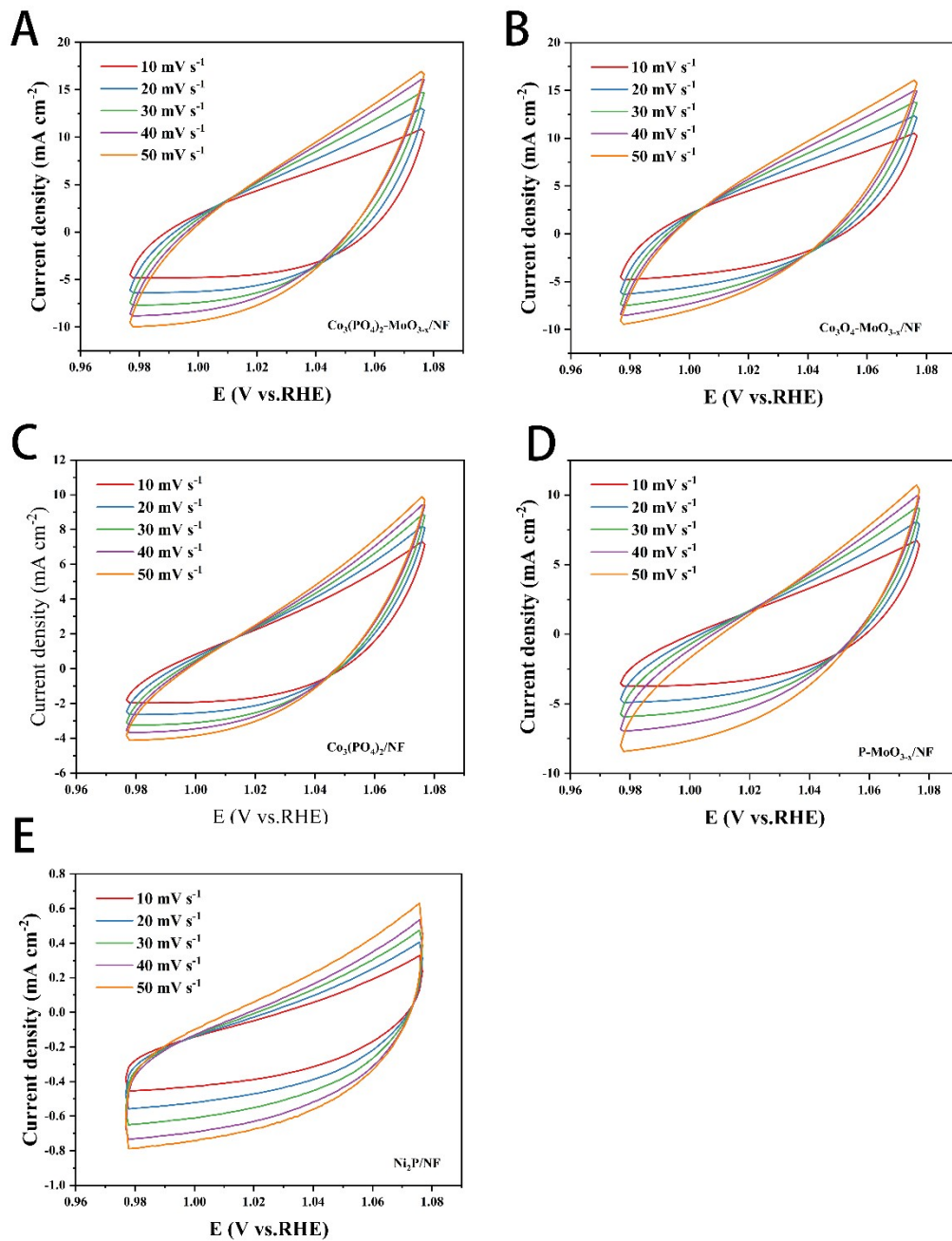
Figure S19. In the OER test, Cyclic voltammograms (CV) curves for (A) Crystalline/amorphous $Co_3(PO_4)_2$-MoO_{3-x}/NF, (B) Co_3O_4-MoO_{3-x}/NF, (C) crystalline $Co_3(PO_4)_2$/NF, (D) amorphous P-MoO_{3-x}/NF, and(E) Ni_2P/NF between 0.97 to 1.97 V vs RHE at five different scan rates (10, 20, 30, 40, and 50 mV/s).
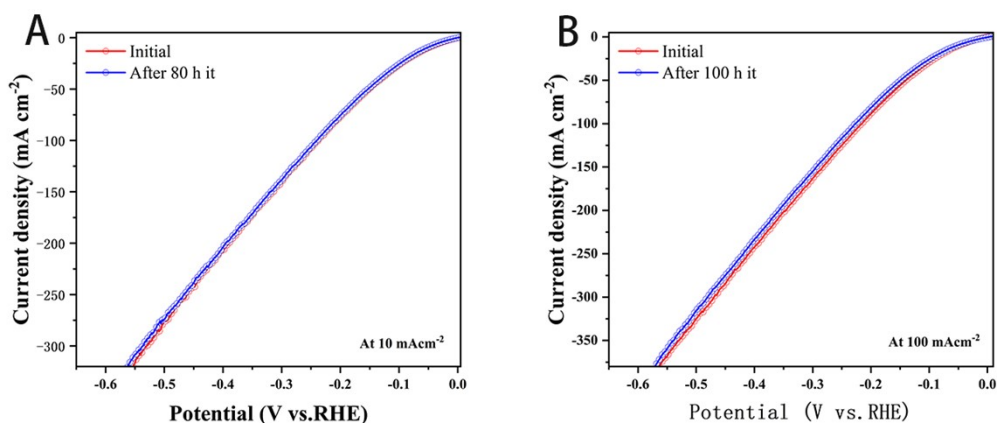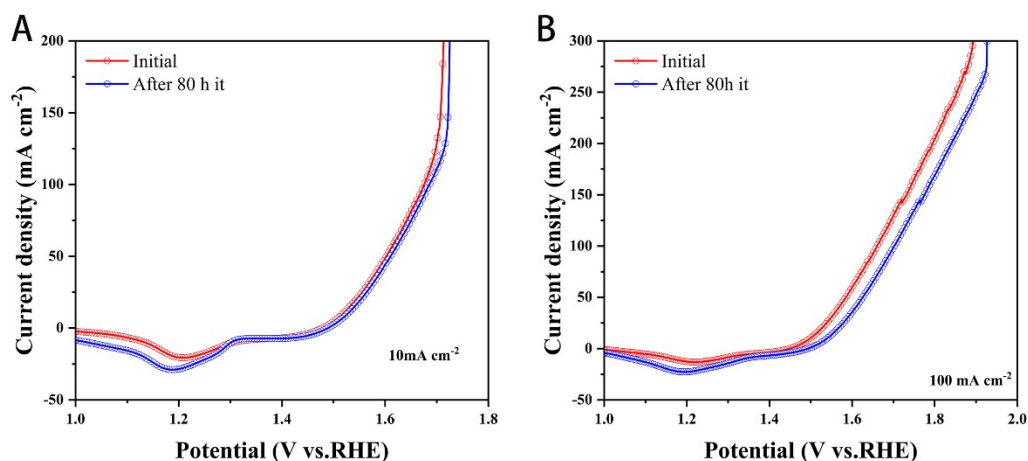
Figure S20. Polarization curves were recorded from $Co_3(PO_4)_2$-MoO_{3-x}/NF heterostructure for OER at a scan rate of 2mV/s initial (red curve) and after (blue curve) the chronopotentiometry test. The current densities corresponding to A and B are 10 and 100 mA cm^{-2} respectively.
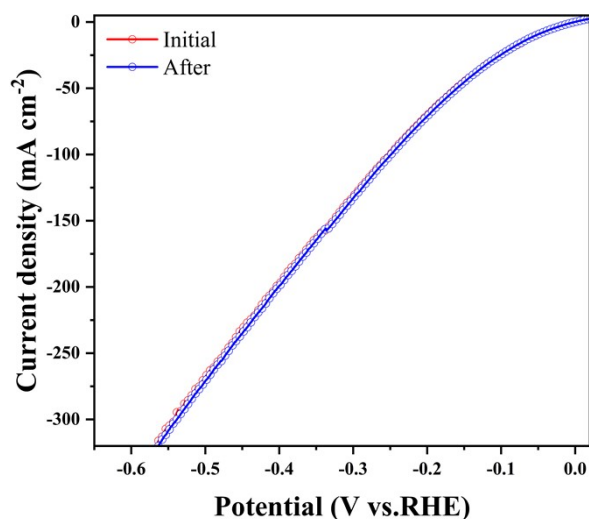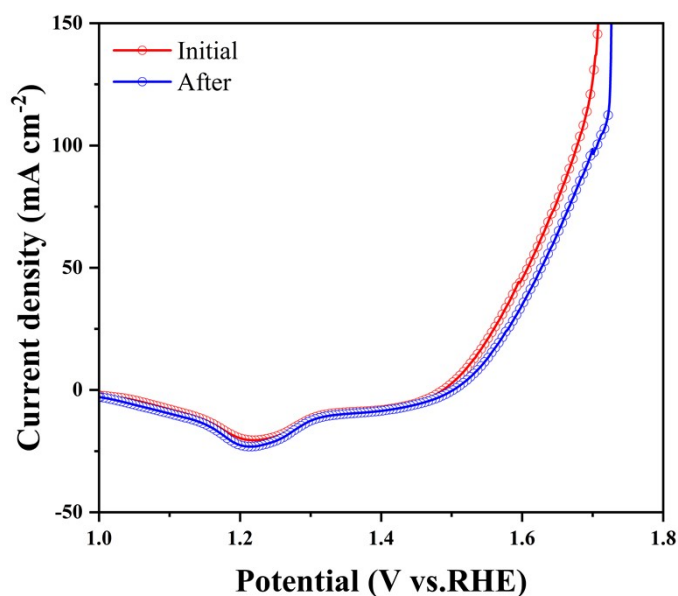

Figure S21. Polarization curves recorded from $Co_3(PO_4)_2$-MoO_{3-x}/NF heterostructure for OER at a scan rate of 2mV/s initial (red curve) and after (blue curve) the Multistep chronopotentiometry test.
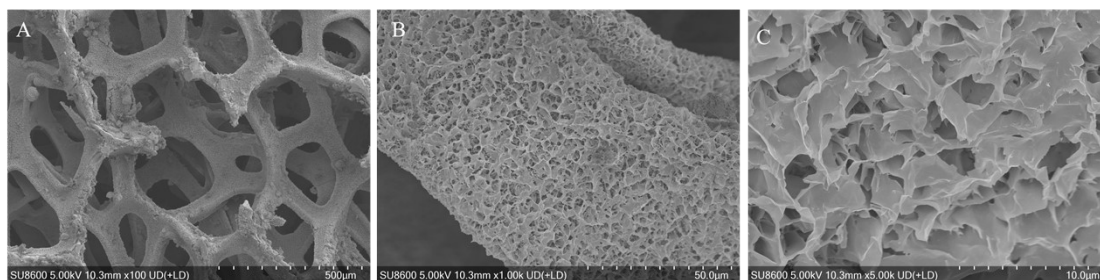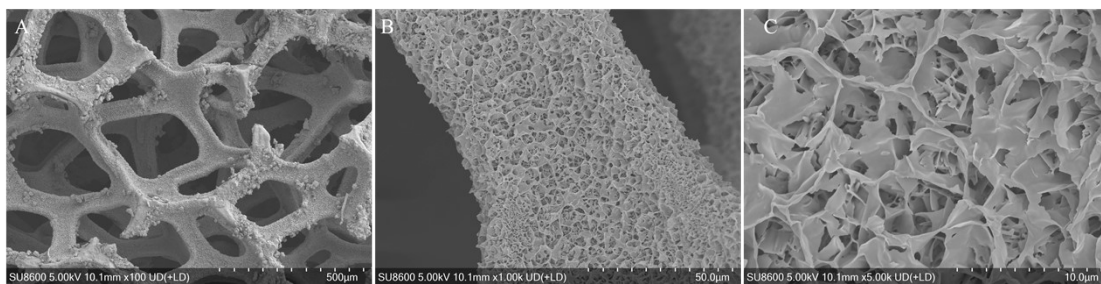
Figure S22. The SEM image of the $Co_3(PO_4)_2$-MoO_{3-x}/NF heterojunction was obtained after the OER stability test.
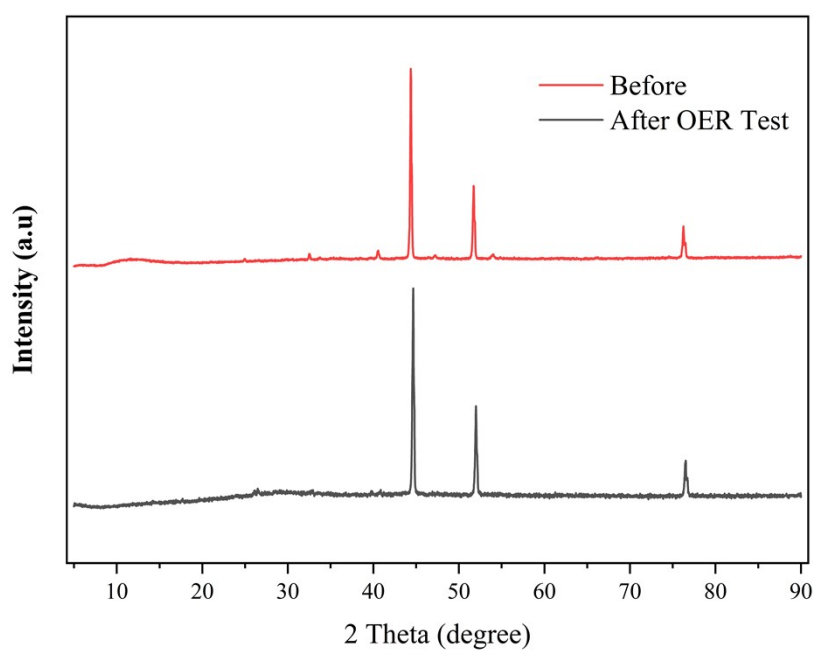
Figure S23. The XRD image of the $Co_3(PO_4)_2$-MoO_{3-x}/NF heterojunction was obtained after the OER stability test.
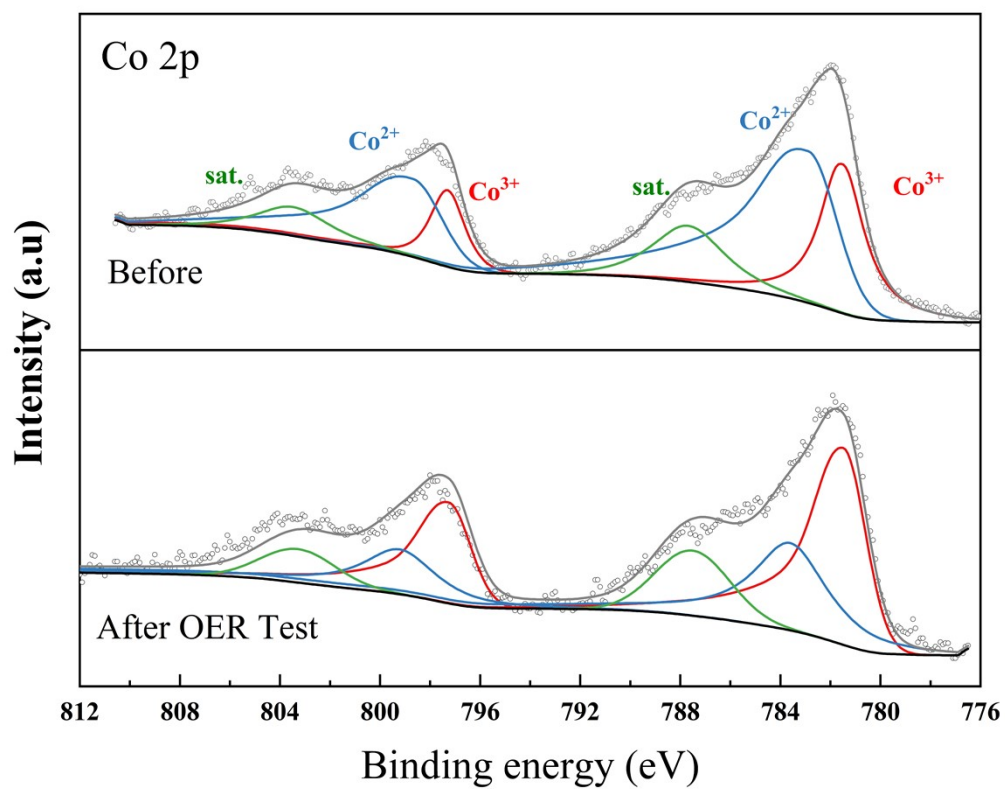
Figure S24. High-resolution XPS spectra of Co 2p for $Co_3(PO_4)_2$-MoO_{3-x}/NF after the OER stability test.
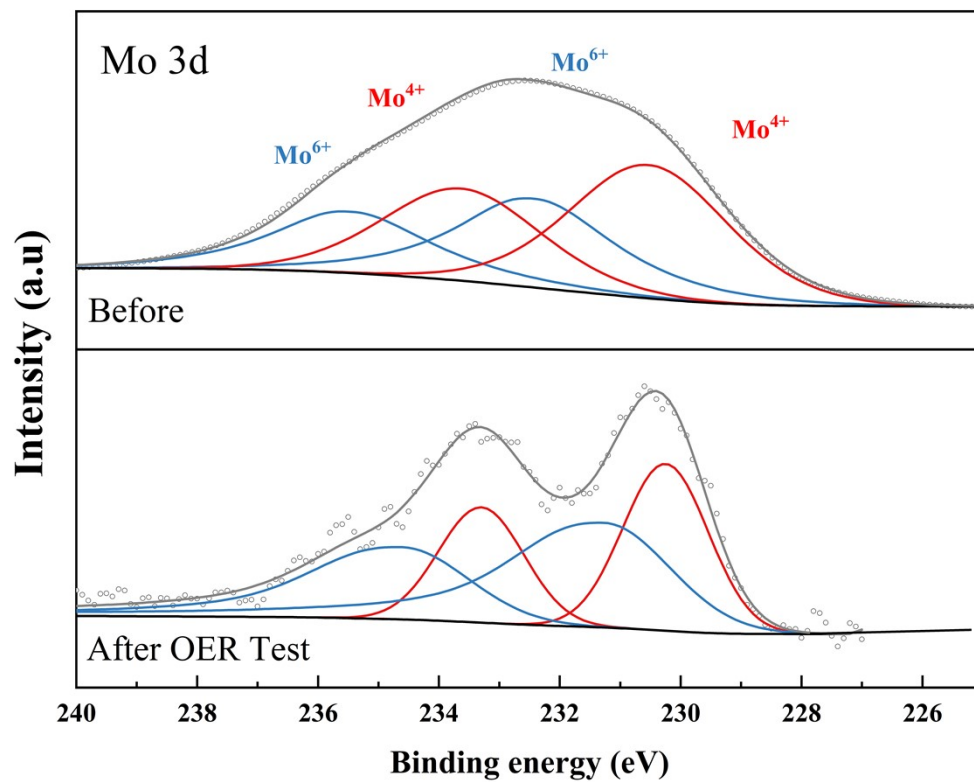
Figure S25. High-resolution XPS spectra of Mo 3d for $Co_3(PO_4)_2$-MoO_{3-x}/NF after the OER stability test.
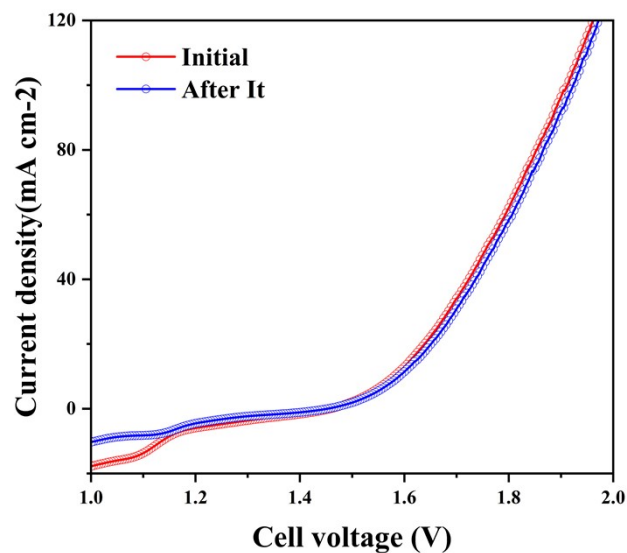
Figure S26. Polarization curves recorded from $Co_3(PO_4)_2$-MoO_{3-x}/NF heterostructure for Overall Water Splitting at a scan rate of 2 mV/s initial (red curve) and after (blue curve) the water splitting chronopotentiometry test.
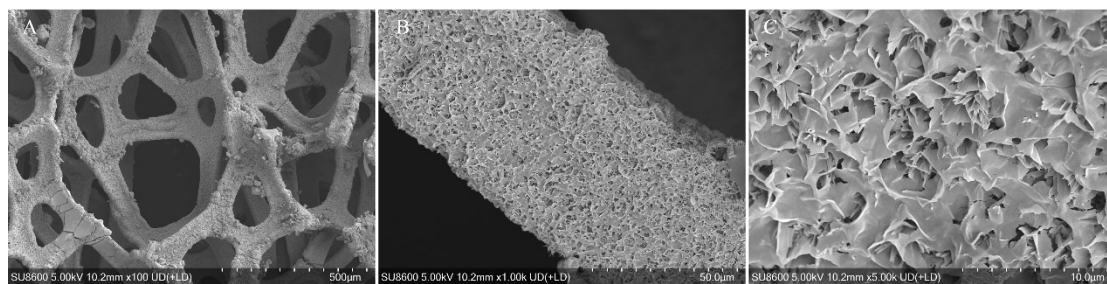
Figure S27. The SEM image of the cathode electrode material in the dual-electrode system subsequent to the stability test.
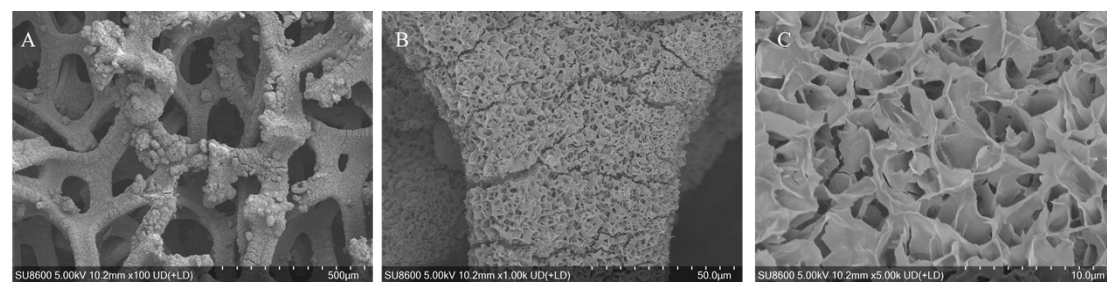
Figure S28. The SEM image of the anode electrode material in the dual-electrode system subsequent to the stability test.

3. Supporting tables

Table S1 Contents of oxygen-containing species from O 1s XPS spectra.

Species	Area %		
	$Co_3(PO_4)_2$-MoO_{3-x}/NF	$Co_3(PO_4)_2$/NF	P-MoO_{3-x}/NF
M-O	17.28	14.63	8.24
Ov	18.67	32.67	38.31
M-OH	36.45	24.68	32.74
P-O	27.1	28.02	20.74

Table S2 Electrocatalytic hydrogen evolution reaction (HER) performance of recent reports based on amorphous-crystalline materials.

Catalysts	$\eta 10$ (mV)	Tafel slope (mV dec^{-1})	Electrolyte	Ref.
$Co_3(PO_4)_2$-MoO_{3-x}/NF	**34**	**44.4**	**1.0 M KOH**	this work
Mo(0.05)-NiCoP	67	86	1.0 M KOH	[4]
Mo-Ni_3S_2/CoFeOH/NF	109	111	1.0 M KOH	[5]
FCN-8P/NF	77	90.6	1.0 M KOH	[6]
$CoNiPO_x$@$V_{3\%}$-Co_4N/NF	53	85.7	1.0 M KOH	[7]
c-$Ni_2P_4O_{12}$/a-$NiMoO_x$/NF	78	84	1.0 M KOH	[8]
CrO_x–Ni_3N	53	76.4	1.0 M KOH	[9]
$FeCo(NiS_2)_4$-C/A	82	69.57	1.0 M KOH	[10]
Cu-(a-$NiSe_x$/c-$NiSe_2$)/TiO_2 NRs	156.9	51.2	1.0 M KOH	[11]
$Ni_3(BO_3)_2$–Ni_3S_2/NF	92	152.3	1.0 M KOH	[12]
a/c-RuO_2/$Ni_{0.85}Se$	58	62	1.0 M KOH	[13]
$NiMoO_x$/NiMoS	38	38	1.0 M KOH	[14]
α-$CoMoP_x$/CF	59	55	1.0 M KOH	[15]
$Ni(OH)_2$–$NiMoO_x$/NF	36	38	1.0 M KOH	[16]
Zn-VO_x-Co	72	75	1.0 M KOH	[17]
Co_4N–CeO_2/NF	52	56.8	1.0 M KOH	[18]
Fe–Ni@NC-CNTs/GC	202	113	1.0 M KOH	[19]
CoP@PS/NCNT	80	53	1.0 M KOH	[20]
Co/WN NWs	151	82	1.0 M KOH	[21]

Table S3 Electrocatalytic oxygen evolution reaction (OER) performance of recent reports based on amorphous-crystalline materials.

Catalysts	Overpotential @current density	Tafel slope (mV dec^{-1})	Electrolyte	Ref.

Co$_3$(PO$_4$)$_2$-MoO$_{3-x}$/NF	**263 mV@10 mA cm^{-2}**	**33.9**	**1.0 M KOH**	**this work**
Mo(0.05)-NiCoP	233 mV@10 mA cm^{-2}	52	1.0 M KOH	[4]
Mo-Ni$_3$S$_2$/CoFeOH/NF	246 mV@10 mA cm^{-2}	33	1.0 M KOH	[5]
FCN-8P/NF	233 mV@10 mA cm^{-2}	44.5	1.0 M KOH	[6]
CoNiPOx@V$_{3\%}$-Co$_4$N/NF	270 mV@10 mA cm^{-2}	54.66	1.0 M KOH	[7]
c-Ni$_2$P$_4$O$_{12}$/a-NiMoO$_x$/NF	250 mV@20 mA cm^{-2}	99	1.0 M KOH	[8]
CrOx–Ni$_3$N$_2$	308 mV@50 mA cm^{-2}	88.2	1.0 M KOH	[9]
Fe$_{10\%}$–Ni$_1$Co$_2$HPi	206 mV@15 mA cm^{-2}	56	1.0 M KOH	[22]
FeCo(NiS$_2$)$_4$-C/A	230 mV@10 mA cm^{-2}	39.62	1.0 M KOH	[10]
Cu-(a-NiSex/c-NiSe2)/TiO2 NRs	339 mV@10 mA cm^{-2}	54.2	1.0 M KOH	[11]
(WO$_2$–Ni$_{17}$W$_3$)/NiFe(OH)$_x$/NF	240 mV@50 mA cm^{-2}	63.5	1.0 M KOH	[23]
NFO-V$_{0.3}$-P	277 mV@20 mA cm^{-2}	45	1.0 M KOH	[24]
Ni$_3$(BO$_3$)$_2$–Ni$_3$S$_2$/NF	217 mV@10 mA cm^{-2}	106.3	1.0 M KOH	[12]
a/c-RuO2/Ni0.85Se	233 mV@10 mA cm^{-2}	48	1.0 M KOH	[13]
NiMoOx/NiMoS	186 mV@10 mA cm^{-2}	34	1.0 M KOH	[14]
a-CoMoPx/CF	305 mV@10 mA cm^{-2}	50	1.0 M KOH	[15]
Ni2P@FePOxHy	220 mV@10 mA cm^{-2}	43	1.0 M KOH	[25]
Co$_2$P@Co/N–C/GC	320 mV@10 mA cm^{-2}	48.8	1.0 M KOH	[26]
Co–Fe–B	298 mV@10 mA cm^{-2}	62.6	1.0 M KOH	[27]

Table S4 Comparison of electrocatalytic overall alkaline water splitting performance of recent reports based on amorphous-crystalline materials.

Anode materials	Cathode materials	Cell potential@10 mA cm^{-2}	Electrolyte	Ref.
Co$_3$(PO$_4$)$_2$-MoO$_{3-x}$/NF	Co$_3$(PO$_4$)$_2$-MoO$_{3-x}$/NF	1.51 V	1.0 M KOH	this work
Mo(0.05)-NiCoP	Mo(0.05)-NiCoP	1.56 V	1.0 M KOH	[4]
Mo-Ni$_3$S$_2$/CoFeOH/NF	Mo-Ni$_3$S$_2$/CoFeOH/NF	1.51 V	1.0 M KOH	[5]
FCN-8P/NF	FCN-8P/NF	1.56V	1.0 M KOH	[6]
CoNiPOx@V$_{3\%}$-Co4N/NF	CoNiPOx@V$_{3\%}$-Co4N/NF	1.52 V	1.0 M KOH	[7]
c-Ni$_2$P4O$_{12}$/a-NiMoOx/NF	c-Ni$_2$P4O$_{12}$/a-NiMoOx/NF	1.545 V	1.0 M KOH	[8]
CrO$_x$–Ni$_3$N	CrO$_x$–Ni$_3$N	1.53 V	1.0 M KOH	[9]
FeCo(NiS$_2$)$_4$-C/A	FeCo(NiS$_2$)$_4$-C/A	1.51 V	1.0 M KOH	[10]
Cu-(a-NiSe$_x$/c-NiSe$_2$)/TiO$_2$ NRs	Cu-(a-NiSe$_x$/c-NiSe$_2$)/TiO$_2$ NRs	1.62 V	1.0 M KOH	[11]

$Ni_3(BO_3)_2$–Ni_3S_2/NF	$Ni_3(BO_3)_2$–Ni_3S_2/NF	1.49 V	1.0 M KOH	[12]
a/c-RuO_2/$Ni_{0.85}$Se	a/c-RuO_2/$Ni_{0.85}$Se	1.488 V	1.0 M KOH	[13]
NiMoOx/NiMoS	NiMoOx/NiMoS	1.46 V	1.0 M KOH	[14]
a-CoMoPx/CF	a-CoMoPx/CF	1.581 V	1.0 M KOH	[15]
Ni_2P@$FePO_xH_y$–$MoNi_4$/MoO_2	Ni_2P@$FePO_xH_y$–$MoNi_4$/MoO_2	1.491 V	1.0 M KOH	[25]
CoMnO@CN	CoMnO@CN	1.7 V	1.0 M KOH	[28]
EO Mo-/Co–N–C/Cu	EO Mo-/Co–N–C/Cu	1.62 V	1.0 M KOH	[29]
Fe–Ni_2P/MoS_x/NF	Fe–Ni_2P/MoS_x/NF	1.61 V	1.0 M KOH	[30]
FeNiB/FeNi	FeNiB/FeNi	1.65 V	1.0 M KOH	[31]
CoP/NCNHP/GC	CoP/NCNHP/GC	1.64 V	1.0 M KOH	[32]

4.Supporting references

[1]   NAZARI M, GHAEMMAGHAMI M. Approach to Evaluation of Electrocatalytic Water Splitting Parameters, Reflecting Intrinsic Activity: Toward the Right Pathway , J. ChemSusChem, 2023, 16(11). https://doi.org/10.1002/cssc.202202126

[2]   ZHAO T, ZHONG D, TIAN L, et al. Constructing abundant phase interfaces of the sulfides/metal-organic frameworks p-p heterojunction array for efficient overall water splitting and urea electrolysis , J. Journal of Colloid and Interface   Science,   2023,   634:   630-41. https://doi.org/10.1016/j.jcis.2022.11.149

[3]   LU J, CHEN S, ZHUO Y, et al. Greatly Boosting Seawater Hydrogen Evolution by Surface Amorphization and Morphology Engineering on MoO2/Ni3(PO4)2 , J. Advanced   Functional   Materials,   2023,   33(51). https://doi.org/10.1002/adfm.202308191

[4]   WANG X, YU M, LV C, et al. Mo-doped NiCoP nanoplates with amorphous/crystalline heterostructure for efficient alkaline overall water splitting , J. FlatChem, 2024, 45. https://doi.org/10.1016/j.flatc.2024.100660

[5]   HOU J, SHENG Y, BI D, et al. Interface engineering of crystalline-amorphous heterostructures with strong electronic interactions for efficient alkaline overall water splitting , J. Journal of Alloys and Compounds, 2024, 977. https://doi.org/10.1016/j.jallcom.2024.173447

[6]   LI H, XIAO Y, TIAN X, et al. A crystalline/amorphous FeCo alloy/FeCoNi-Pi bifunctional electrocatalyst for efficient overall water splitting , J. Inorganic   Chemistry   Frontiers,   2024,   11(12):   3585-95. https://doi.org/10.1039/D4QI00574K

[7]   SINGH T I, MAIBAM A, CHA D C, et al. High‐Alkaline Water‐Splitting Activity of Mesoporous 3D Heterostructures: An Amorphous‐Shell@Crystalline‐Core Nano‐Assembly of Co‐Ni‐Phosphate Ultrathin‐Nanosheets and V‐Doped Cobalt‐Nitride Nanowires , J. Advanced Science, 2022, 9(23). https://doi.org/10.1002/advs.202201311

[8]   WANG J, HU J, NIU S, et al. Crystalline‐Amorphous Ni2P4O12/NiMoOx Nanoarrays for Alkaline Water Electrolysis: Enhanced Catalytic Activity via In Situ Surface   Reconstruction   ,   J.   Small,   2022,   18(10). https://doi.org/10.1002/smll.202105972

[9]   YANG M, ZHAO M, YUAN J, et al. Oxygen Vacancies and Interface Engineering on Amorphous/Crystalline CrOx‐Ni3N Heterostructures toward High‐Durability and Kinetically Accelerated Water Splitting , J. Small, 2022, 18(14). https://doi.org/10.1002/smll.202106554

[10]   GU Z, ZHANG Y, WEI X, et al. Unveiling the Accelerated Water Electrolysis Kinetics of Heterostructural Iron‐Cobalt‐Nickel Sulfides by Probing into Crystalline/Amorphous Interfaces in Stepwise Catalytic Reactions , J. Advanced Science, 2022, 9(30). https://doi.org/10.1002/advs.202201903

[11]   PARK K R, TRAN D T, NGUYEN T T, et al. Copper-Incorporated heterostructures of amorphous NiSex/Crystalline NiSe2 as an efficient electrocatalyst for overall

water splitting , J. Chemical Engineering Journal, 2021, 422. https://doi.org/10.1016/j.cej.2021.130048

[12] SUN Z, WANG X, YUAN M, et al. "Lewis Base-Hungry" Amorphous‑Crystalline Nickel Borate‑Nickel Sulfide Heterostructures by In Situ Structural Engineering as Effective Bifunctional Electrocatalysts toward Overall Water Splitting , J. ACS Applied Materials & Interfaces, 2020, 12(21): 23896-903. https://doi.org/10.1021/acsami.0c03796

[13] LI L, SUN H, XU X, et al. Engineering Amorphous/Crystalline Rod-like Core‑Shell Electrocatalysts for Overall Water Splitting , J. ACS Applied Materials & Interfaces, 2022, 14(45): 50783-93. https://doi.org/10.1021/acsami.2c13417

• [14] ZHAI P, ZHANG Y, WU Y, et al. Engineering active sites on hierarchical transition bimetal oxides/sulfides heterostructure array enabling robust overall water splitting , J. Nature Communications, 2020, 11(1). https://doi.org/10.1038/s41467-020-19214-w

[15] HUANG H, CHO A, KIM S, et al. Structural Design of Amorphous CoMoPx with Abundant Active Sites and Synergistic Catalysis Effect for Effective Water Splitting , J. Advanced Functional Materials, 2020, 30(43). https://doi.org/10.1002/adfm.202003889

[16] DONG Z, LIN F, YAO Y, et al. Crystalline Ni(OH)2/Amorphous NiMoOx Mixed‑Catalyst with Pt‑Like Performance for Hydrogen Production , J. Advanced Energy Materials, 2019, 9(46). https://doi.org/10.1002/aenm.201902703

[17] CHEN M, LIU J, KITIPHATPIBOON N, et al. Zn-VOx-Co nanosheets with amorphous/crystalline heterostructure for highly efficient hydrogen evolution reaction , J. Chemical Engineering Journal, 2022, 432. https://doi.org/10.1016/j.cej.2021.134329

[18] LU M, CHEN D, WANG B, et al. Boosting alkaline hydrogen evolution performance of Co4N porous nanowires by interface engineering of CeO2 tuning , J. Journal of Materials Chemistry A, 2021, 9(3): 1655-62. https://doi.org/10.1039/D0TA08347J

[19] ZHAO X, PACHFULE P, LI S, et al. Bifunctional Electrocatalysts for Overall Water Splitting from an Iron/Nickel‑Based Bimetallic Metal‑Organic Framework/Dicyandiamide Composite , J. Angewandte Chemie International Edition, 2018, 57(29): 8921-6. https://doi.org/10.1002/anie.201803136

[20] LI D J, KANG J, LEE H J, et al. High Activity Hydrogen Evolution Catalysis by Uniquely Designed Amorphous/Metal Interface of Core‑shell Phosphosulfide/N‑Doped CNTs , J. Advanced Energy Materials, 2018, 8(13) https://doi.org/10.1002/aenm.201702806.

[21] LIU Z, ZHANG X, SONG H, et al. Electronic Modulation between Tungsten Nitride and Cobalt Dopants for Enhanced Hydrogen Evolution Reaction at a Wide Range of pH , J. ChemCatChem, 2020, 12(11): 2962-6. https://doi.org/10.1002/cctc.202000391

[22] SHENG H, QU H, ZENG B, et al. Enriched Fe Doped on Amorphous Shell Enable Crystalline@Amorphous Core‑Shell Nanorod Highly Efficient Electrochemical

Water Oxidation , J. Small, 2023, 19(35). https://doi.org/10.1002/smll.20230087

[23] LIU J, QIAN G, YU T, et al. Amorphous-crystalline heterostructure for simulated practical water splitting at high-current‐density , J. Chemical Engineering Journal, 2022, 431. https://doi.org/10.1016/j.cej.2021.134247

[24] DENG H, JIANG H, WANG K, et al. Coupling the vanadium-induced amorphous/crystalline NiFe2O4 with phosphide heterojunction toward active oxygen evolution reaction catalysts , J. Nanotechnology Reviews, 2022, 11(1): 3165-73. https://doi.org/10.1515/ntrev-2022-0450

[25] MEENA A, THANGAVEL P, JEONG D S, et al. Crystalline-amorphous interface of mesoporous Ni2P @ FePOxHy for oxygen evolution at high current density in alkaline-anion-exchange-membrane water-electrolyzer , J. Applied Catalysis B: Environmental, 2022, 306. https://doi.org/10.1016/j.apcatb.2022.121127

[26] ZHU C, FU S, XU B Z, et al. Sugar Blowing‐Induced Porous Cobalt Phosphide/Nitrogen‐Doped Carbon Nanostructures with Enhanced Electrochemical Oxidation Performance toward Water and Other Small Molecules , J. Small, 2017, 13(33). https://doi.org/10.1002/smll.201700796

[27] CHEN H, OUYANG S, ZHAO M, et al. Synergistic Activity of Co and Fe in Amorphous Cox‐Fe‐B Catalyst for Efficient Oxygen Evolution Reaction , J. ACS Applied Materials & Interfaces, 2017, 9(46): 40333-43. https://doi.org/10.1021/acsami.7b13939

[28] LI J, WANG Y, ZHOU T, et al. Nanoparticle Superlattices as Efficient Bifunctional Electrocatalysts for Water Splitting , J. Journal of the American Chemical Society, 2015, 137(45): 14305-12. https://doi.org/10.1021/jacs.5b07756

[29] SHI H, DAI T Y, WAN W B, et al. Mo‐/Co‐N‐C Hybrid Nanosheets Oriented on Hierarchical Nanoporous Cu as Versatile Electrocatalysts for Efficient Water Splitting , J. Advanced Functional Materials, 2021, 31(28). https://doi.org/10.1002/adfm.202102285

[30] ZHANG X, LIANG C, QU X, et al. Sandwich‐Structured Fe‐Ni2P/MoSx/NF Bifunctional Electrocatalyst for Overall Water Splitting , J. Advanced Materials Interfaces, 2020, 7(12). https://doi.org/10.1002/admi.201901926

[31] YUAN H, WANG S, GU X, et al. One-step solid-phase boronation to fabricate self-supported porous FeNiB/FeNi foam for efficient electrocatalytic oxygen evolution and overall water splitting , J. Journal of Materials Chemistry A, 2019, 7(33): 19554-64. https://doi.org/10.1039/C9TA04076E

[32] PAN Y, SUN K, LIU S, et al. Core‐Shell ZIF-8@ZIF-67-Derived CoP Nanoparticle-Embedded N-Doped Carbon Nanotube Hollow Polyhedron for Efficient Overall Water Splitting , J. Journal of the American Chemical Society, 2018, 140(7): 2610-8. https://doi.org/10.1039/C9TA04076E